

Origin of scaling structure and non-gaussian velocity distribution in self-gravitating ring model

Yasuhide Sota^{1;3}, O사무 Iguchi¹, Masahiro Morikawa¹^y,
 Takayuki Tatekawa²^{yy}, and Keiichi Maeda^{2;3;4}^z

¹ Department of Physics, Ochanomizu University, 2-1-1 Ohtuka, Bunkyo, Tokyo, 112-8610 Japan

² Department of Physics, Waseda University, Shinjuku, Tokyo 169-8555, Japan

³ Advanced Research Institute for Science and Engineering, Waseda University, Shinjuku, Tokyo 169-8555, Japan

⁴ Advanced Institute for Complex Systems, Waseda University, Shinjuku, Tokyo 169-8555, Japan

Abstract

Fractal structures and non-Gaussian velocity distributions are characteristic properties commonly observed in virialized self-gravitating systems such as galaxies or interstellar molecular clouds. We study the origin of these properties using the one-dimensional ring model which we newly propose in this paper. In this simple model, N particles are moving, on a circular ring fixed in the three dimensional space, with mutual interaction of gravity. This model is suitable for accurate symplectic integration method by which we find the phase transition in this system from extended-phase to collapsed-phase through an interesting phase (halo-phase) which has negative specific heat. In this intermediate energy scale, there appear scaling properties, non-thermal and non-Gaussian velocity distributions. In contrast, these peculiar properties are never observed in other gas and core phases. Particles in each phase have typical time scales of motion determined by the cutoff length, the ring radius R and the total energy E . Thus all relaxation patterns of the system are determined by these three time scales.

I. INTRODUCTION

Many astrophysical objects in our universe are composed of mutually interacting elements through gravity. If they are almost isolated systems, they are called self-gravitating systems (SGS). For example, galaxies, clusters of them, globular clusters and molecular clouds are thought to be typical SGS. Their statistical properties are often characterized by non-Gaussian velocity (or pairwise velocity) distributions [1], fractal structures [2], and the scaling relation between a mass-density and a system size [3]. Most of these objects are thought to be in gravitationally virialized quasi-equilibrium state. Therefore the pure gravitational force, among other forces and initial conditions, seems to play an essential role in characterizing above statistical properties of SGS.

There have been some theoretical approaches to explain fractal structures in SGS from the viewpoint of criticality and phase transition in gravo-thermodynamics [4]. Strictly speaking, the ordinary SGS in three-dimension (3-D) cannot attain the genuine stable equilibrium, because the gravitational force does not vanish at long distances (IR-divergence) and diverges at short distances (UV-divergence). These properties of the gravity cause the gravothermal catastrophe in the self-gravitating gas system enclosed in a solid adiabatic wall. In fact, the isothermal sphere as a solution of the saddle point limit for the

^xE-mail:sota@skyrise.phys.socha.ac.jp

^yE-mail:samu@phys.socha.ac.jp

^{yy}E-mail:hiroy@gravity.phys.waseda.ac.jp

^zE-mail:maeda@mse.waseda.ac.jp

microcanonical partition function is not always stable, since the entropy does not necessarily take the local maximum for its solution [5,7]. Therefore the introduction of a small-scale cut-off as well as a large-scale cut-off had been inevitable in order to discuss the equilibrium state for such unstable systems. Though the introduction of the cut-off prevents the gravothermal catastrophe, 3-D gravitational system has a phase with negative specific heat treated in the microcanonical ensemble [8]. Even in the canonical ensemble, this system is highly unstable. When the temperature is reduced, the system experiences a violent first-order phase transition from the gas phase into the cluster phase. According to these arguments, no stable equilibrium state is expected for 3-D gravitational system with or without cut-off in any ensemble.

On the other hand in the real world, we won't expect genuine equilibrium but quasi-equilibrium states which is expected to appear in dynamical description such as collision-less Boltzmann equation. Finite lifetime of such structures is sufficient to explain the present structures of SG S even if they are expected to evolve further into different quasi-stable state through two-body relaxation.

The relaxation process of SG S is mainly discussed within the one-dimensional gravitational sheet model (1D S) [10,11]. In this model, many parallel sheets interact with each other through the constant force which never decays at distant places. Though the interaction is long-ranged, no phase transition occurs. Thermodynamics of 1D S is exactly solved and actually, in the numerical calculations, the system reaches the thermodynamic equilibrium long after it attains virial equilibrium. In this model, the virial condition gives the relation $2\langle K_i \rangle = \langle V_i \rangle$ between the time averaged kinetic energy $\langle K_i \rangle$ and the time averaged potential energy $\langle V_i \rangle$. Therefore, contrary to the 3-D SG S, the specific heat in 1D S is always positive. Thus its relaxation process is quite different from that in 3-D SG S. Another well-known one-dimensional model which has long-range force is the Hamiltonian mean field (HMF) model, in which a phase transition occurs [12]. There have been a lot of studies on the relaxation process for HMF. In fact, it is known that Levy type motion of constituent particles and super-diffusion process occur in HMF [13]. However, its interaction form is also quite different from that of real 3-D gravitational system, even if it reaches a virial equilibrium. Actually, the specific heat is always positive and the phase transition is second-order.

Seeking for much faithful model representing the 3-D SG S, several simple models have been proposed [14]. For example the cell model and its extended version are among the simplest models to possess the property of phase transition. In these models, the pair potential for the interaction takes constant values both inside and outside the cells [15,16]. At the low temperature, most particles are trapped in several clusters, while they escape and move freely at higher temperatures. However, it seems difficult to examine the relaxation process of this system numerically, since the interaction is not efficient to cause relaxation; particles have no interaction within each cell. There are also several numerical analysis with the different type interactions including the lower and higher cut-offs [16,17]. However, the value of the cut-off among these models seems too large to see the intrinsic properties of the real 3-D SG S.

In summary, it seems important to propose a toy model which reflects a property of the negative specific heat and a phase transition of 3-D self-gravitating system and to analyze what kinds of quasi-equilibrium states exist in it before it reaches thermodynamic equilibrium.

In this paper, we propose a new model (Self-Gravitating Ring: SGR) which has a) negative specific heat, b) shows phase transition representing 3-D SG S and c) numerically tractable. The system in this model consists of N particles mutually interacting through 3-D gravity but are constrained on a ring with a fixed radius. The force is genuine 3-D gravity and the calculation is essentially one-dimensional. Moreover, the Hamiltonian permits a powerful symplectic integration method by which we can analyze the nature of quasi-equilibrium states and phase transition in this model.

In section II, we introduce the SGR model, then classify the quasi-equilibrium state into three states including the state with the negative specific heat in section III. In sections IV, V, and VI, we analyze the particle motions from a statistical point of view, and study the scaling structure of a formed cluster and see the tendency of a relaxation toward thermodynamic equilibrium. Finally, we will discuss our results in section VII.

II. SELF-GRAVITATING RING MODEL

In this section, we introduce a self-gravitating ring (SGR) model, in which particles interact with each other through genuine 3-D gravity while the particle configuration is constrained on a 1-D ring. By utilizing this model, we expect to study the gravitational phase transition, which was impossible in

the 1D S model [11]. This is because the potential of 1D S model increases linearly without bound, and therefore there is no characteristic energy scale required for a particle to escape; we have the bound and the characteristic energy scale in our SG R model.

We consider a system of self-gravitating N particles with mass m , whose motions are smoothly constrained on a circular ring with a fixed radius R without friction (Fig.1). Each pair of particles interacts with each other through 3-D gravitational force. The distance between a pair is measured by the length of the straight line combining the pair and not by the minor arc of the ring.

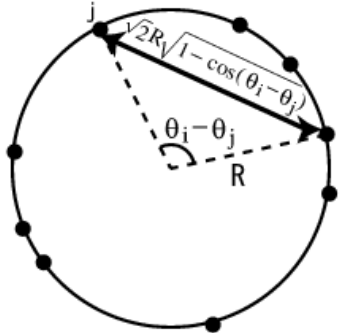


FIG.1. Picture of SG R model with a fixed radius R . The particle at a position i receives a 3-D gravitational force from the particle at a position j . The force follows an inverse square law for the distance between the two particles which is shown as a straight line in the picture.

The Hamiltonian of this system becomes

$$H_p = \frac{1}{2mR^2} \sum_{i=1}^N \dot{p}_i^2 - \sum_{i < j} \frac{Gm^2}{2R} \frac{1}{1 - \cos(\theta_i - \theta_j)}: \quad (2.1)$$

The position of i -th particle is fully described by the angular variable θ_i as $r_i = (R \sin \theta_i; R \cos \theta_i)$, and is a UV-cuto parameter and the momentum conjugate to θ_i is given by $\dot{p}_i = mR^2 \dot{\theta}_i$. This cut-off actually truncates the diverging gravitational force at the distance $2R$.

We first introduce three dynamical time-scales apparently included in the above Hamiltonian. They are parameterized by the ring radius R , the cut-off scale r , and the total energy E of the system.

When the system is almost uniformly filled by moving particles, we have the longest dynamical time t_R defined by

$$t_R = \frac{r}{\frac{R^3}{GNm}}: \quad (2.2)$$

During this time t_R , a typical particle goes around the ring once. Therefore, the time when the whole system attains thermodynamic equilibrium, if any, is at least larger than this time scale.

When particles collapsed completely into a core, we find the shortest dynamical time-scale t defined as

$$t = \frac{r}{\frac{3}{GNm}}: \quad (2.3)$$

During this time t , a typical particle bounded in the core oscillates once.

There is yet another time scale which falls in between the above mentioned two extreme time scales. Suppose that the system is stably confined in a scale r which satisfies

Note that we will classify the particles with three species, core, halo, and gas species in the next section and show that the typical time scale t_R and t are characteristic for the particles in gas and core species, respectively.

$$< < r < < R : \quad (2.4)$$

In this region, the ring can be approximated as an infinite straight line and the cutoff can be neglected. Then the leading term of the denominator of the potential term in the Hamiltonian (2.1) becomes $(i - j)^2$ and

$$H = \frac{1}{2m R^2} \sum_{i=1}^N \frac{p_i^2}{R} + \sum_{i < j} \frac{G m^2}{R j_i j_j} : \quad (2.5)$$

In this case, the potential term V_p satisfies Euler's theorem for homogeneous function,

$$\sum_{i=1}^N \frac{\partial V_p}{\partial p_i} = V_p : \quad (2.6)$$

and the ordinary virial condition holds

$$2 \langle K_p \rangle = \langle V_p \rangle ; \quad (2.7)$$

where angle-brackets represent the long-time average.^y In this virial condition, the typical size of a system, r is related with the total energy E as

$$E = \frac{V_p}{2} = \frac{G m^2 N^2}{4r} : \quad (2.8)$$

Hence the above condition for r (2.4) reads as

$$\frac{G m^2 N^2}{4} = E j = \frac{G m^2 N^2}{4R} : \quad (2.9)$$

Further from the virial condition, the velocity dispersion is estimated as

$$2 \langle K_p \rangle = \langle V_p \rangle = m N \langle v^2 \rangle ; \quad (2.10)$$

where $v = dr/dt$ and therefore

$$p \frac{r}{\langle v^2 \rangle} = \frac{r}{\frac{2E}{mN}} : \quad (2.11)$$

From this equation (2.11), the crossing time is defined as

$$t_E = \frac{r}{\langle v^2 \rangle} = \frac{G m^2 N^2}{4 \frac{E}{2}} : \quad (2.12)$$

This is the intrinsic time scale associated with 3-D SGR model independent neither of the cutoff nor of the volume limit in which the system is confined. Note that this is a unique time scale in 1D S model.^z

The above introduced cutoff parameter connects the two limiting theories in the following sense. In the limit $\epsilon \rightarrow 0$, the SGR model becomes genuine 3-D gravity at the small scale. On the other hand in the limit $\epsilon \rightarrow R$, the model resembles the mean field (HMF) model. This is because, in this limit, the force vanishes at $\epsilon = k$ ($k = 0, 1, \dots$) and takes $\epsilon = R$, the maximum finite value at $\epsilon = (k+1)^2$ ($k = 0, 1, \dots$), where the curvature of the potential is equal to the value at $\epsilon = k$ for both of these models.

^y Outside of the above region in SGR model, this form of virial relation is modified even in the limit of $\epsilon \rightarrow 0$, as is shown in Appendix A.

^z As we will show in Sec. IV, this is also the time scale for the particles in halo species in SGR model.

For numerical simulations, we need to make all physical variables non-dimensional; we use m , R , and t_R for the unit of mass, distance, and time, respectively. In these units, the physical Hamiltonian (2.1) reads

$$H_p = G m^2 \frac{N}{R} H ; \quad (2.13)$$

where

$$H = \frac{1}{2} \sum_{i=1}^N \frac{x_i^2}{p_i^2} + \frac{1}{2N} \sum_{i < j} \frac{1}{1 - \cos x_{ij}} ; \quad (2.14)$$

and the dimensionless momentum p_i is given by $p_i = d = d$ and the dimensionless time t is introduced as $t = \frac{t_R}{R}$. The numerical calculations of this Hamiltonian form permit us to use a powerful symplectic integrator [18], with which the total energy is conserved with extremely high accuracy, even beyond thousands of dynamical time. Typical magnitudes of errors for total Hamiltonian $H(t)$ and total momentum $P(t)$ in our following simulations up to 10^4 , are $(H(t) - H(0)) = H(0) \approx O(10^5)$ and $P(t) = P_{rms}(t) \approx O(10^8)$, respectively, where $P_{rms}(t) = \sqrt{\frac{1}{N} \sum_{i=1}^N p_i^2}$.

III. CLASSIFICATION OF PHASES AND PARTICLES

We now study the quasi-equilibrium states that would appear as transient stationary states in our system. Though these states would not be the absolutely stable states as are realized in the ordinary thermodynamics, we are interested in unique properties observed in these transient states. Furthermore, we know right from the beginning the SG S is unstable and this instability becomes apparent in the negative specific heat of the system in the below. Therefore only the transient description is sufficient and necessary to explain observations if the quasi-equilibrium state lasts sufficiently long.

A. Negative specific heat of SG S

First, we study the phase diagram of SG R model in the temperature-energy plane. The T - U relation is presented in Fig 2 and we observe that the negative specific region, i.e. negative slope region, apparently appears. The temperature T and the internal energy per particle U of the present system are defined respectively by

$$T = \frac{2hK(t)}{N} ; \quad (3.1)$$

$$U = \frac{H}{N} ; \quad (3.2)$$

In the above, the internal energy U is conserved in the present microcanonical system, while the temperature T is defined from the kinetic energy $K(t)$ of the system at time t and $hK(t)$ denotes its time averaging from initial time to t . In this paper, we fix the total number of particles $N = 100$ for simplicity and therefore the remaining relevant parameters which characterize the quasi-equilibrium state of the system are T and U .

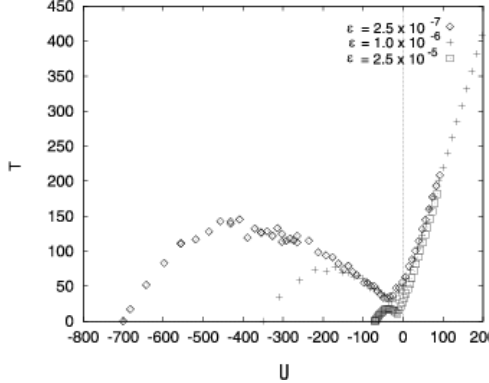


FIG. 2. Diagram of temperature T vs. energy per particle U for three different cutoffs $\epsilon = 2.5 \times 10^{-7}$, 1.0×10^{-6} ; and 2.5×10^{-5} . In each T - U curve, there are two critical energy scales, $U_{c\text{-low}}$ () and $U_{c\text{-high}}$ (), between which the negative specific heat $\partial U = \partial T < 0$ appears.

From Fig. 2, we find two characteristic energy scales where $\partial T = \partial U = 0$; $U_{c\text{-low}}$ () at a low energy side and $U_{c\text{-high}}$ () at a high energy side. The energy scale $U_{c\text{-high}}$ () corresponds to a mean gravitational binding energy per particle, which is estimated as $U_{c\text{-high}} = \frac{1}{2N} \frac{p^2}{2N} \frac{1}{1 - \cos \phi} \quad (N(N-1)=N=0)$, while, $U_{c\text{-low}}$ () strongly depends on the cutoff ϵ . This cutoff dependence would be estimated from the condition (2.9) which, in our normalization, becomes

$$\frac{1}{4} \frac{p^2}{2} = U \quad \frac{1}{4} : \quad (3.3)$$

Under this condition, the negative specific heat condition in virialized state would be justified. Actually, substitution of three different cutoffs $\epsilon = 2.5 \times 10^{-7}$, 1.0×10^{-6} and 2.5×10^{-5} into (3.3) yields the lower limits of (3.3) 353, 177, and 35.3, respectively. Thus the condition (3.3) correctly describes the region of negative specific heat in Fig. 2 with sufficient accuracy. However, the slope of each T - U line in Fig. 2 is less steep than the value -2 which is expected for the virial condition of 3-D gravity. This is probably because the energy range satisfying the condition (3.3) is too narrow for the ideal T - U curves according to our choice of the cutoff parameters; though the slope of a T - U curve would fit the value -2 for the smaller value of ϵ , even the smallest cutoff we took is not yet enough to make the relation converge.

In the range between these two energy scales, i.e. $U_{c\text{-low}} < U < U_{c\text{-high}}$ (), the system has the negative specific heat, which suggests the existence of a phase transition [8,15{17]. Actually in the system with the negative specific heat, a slight energy injection from outside decreases the system's temperature and induces further energy flow from outside. Then this catastrophic temperature reduction induces rapid cluster formations in the system. As we will see soon below, such a phase transition from the gaseous state to the cluster state in fact appears and characteristic structures are realized in this intermediate energy range.

B. Three phases in SG R model

As is seen in Fig. (2), there are apparently three phases classified by the energy per particle U ; a) low energy collapsed phase (C-phase) $U < U_{c\text{-low}}$ (), b) intermediate energy phase (I-phase) $U_{c\text{-low}} < U < U_{c\text{-high}}$ (), and c) high energy gaseous phase (G-phase) $U_{c\text{-high}} < U$. The G-phase (c) is stabilized by the infrared cutoff ($\epsilon = 2$, or a largest physical scale R), without which the particle would travel into spatial infinity. The C-phase (a) is stabilized by the ultraviolet cutoff ϵ , without which the particle would fall into a singularity. The specific heats for these particles are positive, in accord with stability. On the other hand, the I-phase (b) is the most specific to gravity; it is the negative specific heat region and therefore unstable. The nature of this phase is independent of any artificial cutoffs and therefore is thought to represent intrinsic properties of gravity.

The existence of three different phases, as is explained above, distinguishes the SG R model from other models with a long-range force. For example, HMF model has only high and low energy phases, and

shows the second-order phase transition between these phases. On the other hand in SG R model, the intermediate phase with the negative specific heat exists and is strongly unstable when the system is in contact with a heat bath. Therefore the phase transition exists. As for 1D S model, only a single phase exists because the system has no characteristic energy scale; there is no phase transition in this model.

The limit $\tau \rightarrow 0$ in SG R model represents genuine gravity without collision and the range of the intermediate phase increases without bound.

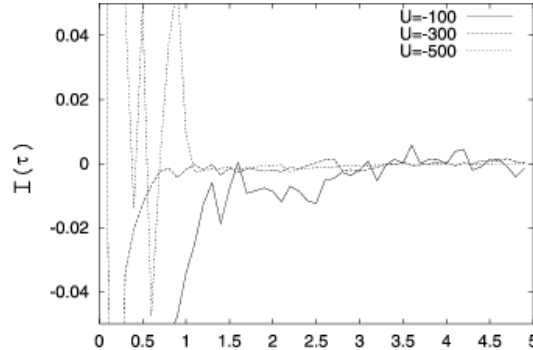


FIG. 3. The time evolution of $I(t)$ defined by the left side of (A5) in the case with $U = 100, 300, 500$ and $\tau = 2.5 \times 10^7$. In each case, the system becomes virial-equilibrium within few dynamical time.

C. Three species: gas, halo, and core particles

In each phase, the particles of the system spread in various energy ranges. For example, in the intermediate phase, some particles evaporate from a cluster and move along a ring almost freely with the time scale τ_R , while some of others fall into the center of the cluster and oscillate with the time scale τ . Thus, the overall phase information does not specify the nature of individual particles. In order to obtain much fine information, we define three species of particles in each phases by using the energy of the particles: the energy of the i 'th particle is given by

$$E_i = \frac{1}{2} p_i^2 - \frac{1}{2N} \sum_{j \neq i}^N \frac{1}{1 - \cos \theta_{ij}}: \quad (3.4)$$

The classification is a) core particles for $E_i < U_{c-low}(t)$, b) halo particle for $U_{c-low}(t) < E_i < U_{c-high}(t)$, and c) gas particle for $U_{c-high}(t) < E_i$.^x

^x Note that even in the C-phase, there exist a few gas particles. We call the core particles and halo particles as cluster in this paper; they form apparent one bound state.

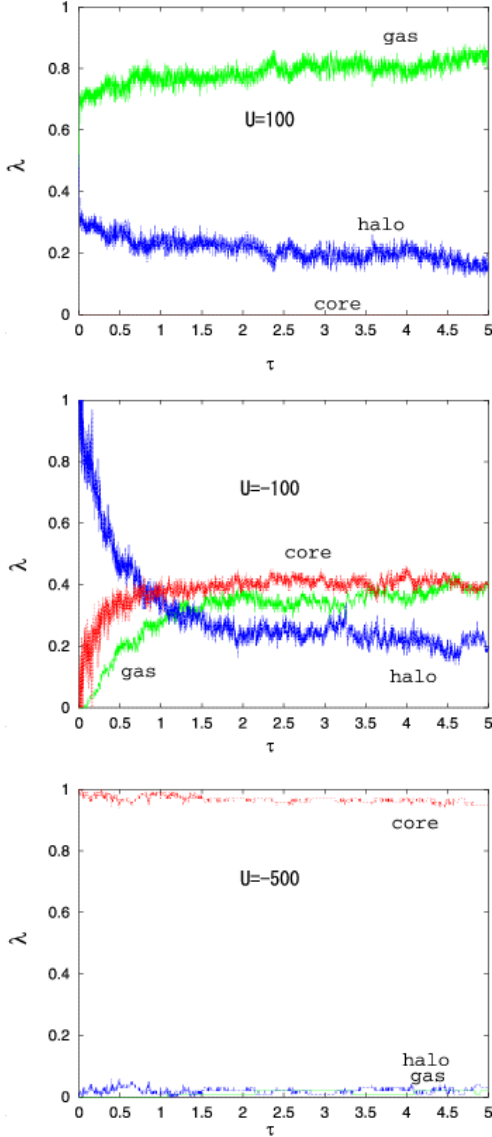


FIG . 4. The time evolution of the percentage of each species; core, halo, and gas in high-energy (G →) phase (top), in intermediate (I →) phase (middle), and in low-energy (C →) phase (bottom) for $\gamma = 2.5 \cdot 10^7$. Gas particles dominate in the high-energy phase, and core particles dominate in the low-energy phase. On the other hand in the intermediate phase, all three species coexist.

In the low temperature phase of SG R, the quasi-equilibrium state at very low temperature is inhomogeneous and only one cluster exists. Most particles are condensed there and the total potential becomes deep. In the intermediate phase, many particles locate around the cluster. As the temperature increases in this phase, halo particles gradually dominate core particles. As the temperature increases further, there also appear gas particles, which evaporate from a cluster and go along the ring. At very high temperature, all particles move almost freely.

We describe the ratio of particle number in each species by core, halo, and gas, which satisfies $\text{core} + \text{halo} + \text{gas} = 1$. Their evolution is in Fig.4, for the case $\gamma = 2.5 \cdot 10^7$. From these figures, we observe that ratios have approached asymptotic values beyond $\gamma = 1$: core ≈ 0 , halo ≈ 0.2 , and gas ≈ 0.8 for $U = 100$ (G phase), core ≈ 0.41 , halo ≈ 0.23 , and gas ≈ 0.36 for $U = -100$ (I phase), core ≈ 0.96 , halo ≈ 0.02 , and gas ≈ 0.02 for $U = -500$ (C phase). In G phase and C phase, gas particles and core particles are dominated in number respectively, while in I phase, all of the three species of particles coexist almost equally. This coexistence is not due to the finiteness of particles ($N = 100$ in this paper) but due to the prominent property of SG S.

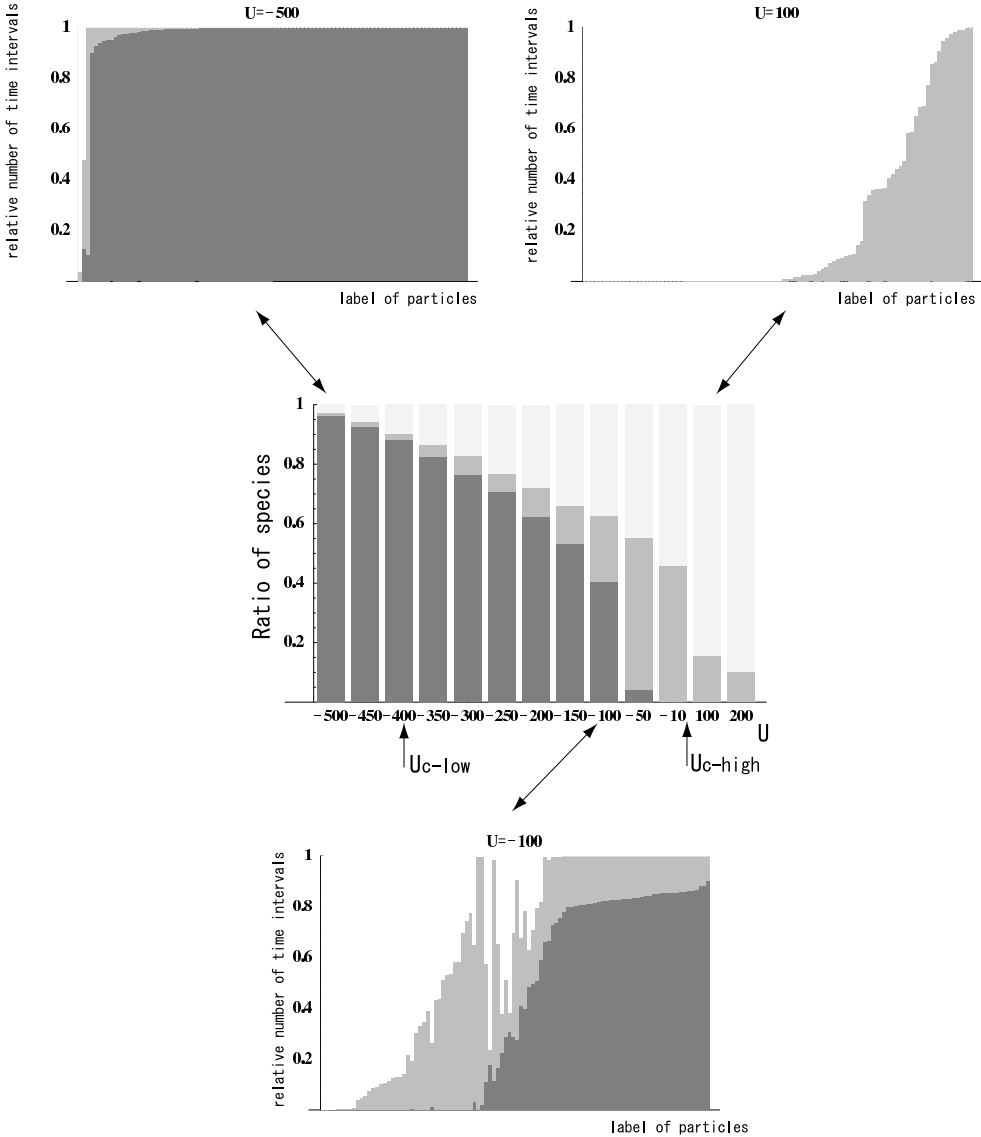


FIG. 5. The figure at a center shows the energy dependence of the ratio of each species in $\tau = 5$ for $\tau = 2.5 \times 10^7$. For the case of three cases, $U = 100$, 100 , and -500 , the ratio of time duration intervals of three states in which each particle stays until $\tau = 5$ is shown around it. The each point in the horizontal axis corresponds to each particle, and each ratio of gas, halo, and core state is represented by white, gray, and black region, respectively. In the both G-phase and C-phase, most particles stay in one state. On the other hand, in the I-phase ($U = -100$), many particles experience at least two states. Some particles wander from one state to another in three states.

In Fig. 5, the energy dependence of the ratio of each species in $\tau = 5$ for $\tau = 2.5 \times 10^7$ is shown at center. The energy scale where halo particles exit corresponds to the one where the negative specific heat appears (I-phase). Together with it, the relative ratio of time intervals of three states in which each particle stays until $\tau = 5$ is shown. As we expect, in both G- and C-phase, most particles stay just in one state for a quite long time. For the I-phase, however, many particles experience at least two states. Some particles wander from one state to another in three states.

IV. PARTICLE MOTIONS

In this section, we examine individual particle motion and velocity distribution function in each phase.

A . R ecurent m otion of halo particles

In the HM F model at the state near the critical energy, Levy-type flight and anomalous diffusion of particles has been reported [13]. These peculiar behaviors of particles are apparently caused by the transitions of particles between core and gas. We would like to emphasize that such peculiar behaviors are caused by the periodicity of the configuration space and not by the long range force itself. In fact, for all Levy-type flights numerically shown in HM F, the flight distances turn out to be longer than the period 2. Therefore the artificial periodicity in the potential, and not the long-range nature of the force itself, is thought to have caused the Levy-type flight in HM F model. In our SG R model, we do have the possibility to observe the same Levy-type flight motions since particles in SG R also move along a closed ring. Since we would like to extract the intrinsic property of the long-range nature of the gravity itself, we would pay our attention to the recurrent motion of halo particles and disregard the round-trip motion along the entire ring.

First, we choose the parameters as $7:1 \quad 10^4 R$ and $U = 100$ for which the system is in the intermediate energy phase. The particle motion is shown in Fig.6(a), in which core particles regularly oscillate around the center of a cluster with the time scale τ and halo particles move-out and move-into the core region without any typical time scale and amplitude. Zoomed in ten-times, the motion is in Fig.6(b), in which we find similar recurrent motions of particles. Further zoomed in ten-times, the motion is in Fig.6(c), in which we find still similar recurrent motions of particles. These repetition of the similar recurrent pattern suggests a self-similar structure of the system.

Note that the recurrent motion of halo particles is confined within the range $[0;2]$ and particles never experience the round-trip along the ring, quite contrary to the HM F model. Moreover, this recurrent motion of particles are quite robust and is observed in any region of the intermediate energy phase. This robustness is a remarkable contrast to the HM F model in which such motion is observed at the critical point in the phase diagram.

In order to analyze this behavior more quantitatively, we examine the frequency distribution of the recurrent time t_{rec} in t_{out} , that is the time period from the moment t_{out} when a particle leaves the barycenter of the core to the moment t_{in} when it returns to the barycenter again. Here we have defined the location of the barycenter of the core as

$$\frac{\sum_{i_c=1}^{N_c} i_c}{N_c} = \bar{x}_c \quad (4.1)$$

where i_c is the location of i_c 'th particle in the core and N_c is the total number of core particles at each moment.

Smaller the cutoff ϵ , larger the range of recurrent motion.

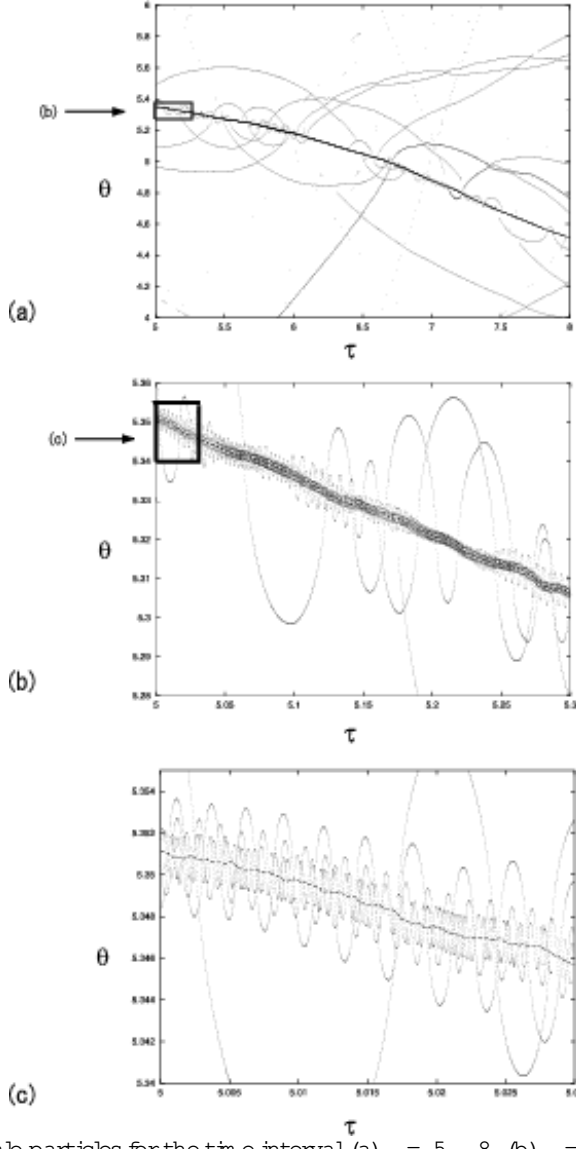


FIG .6. Trajectories of halo particles for the time interval (a) $\tau = 5 \dots 8$, (b) $\tau = 5 \dots 5.3$ and (c) $\tau = 5 \dots 5.03$. Zooming up the marked square region in (a) ten-times yields (b). Further zooming up the marked square region in (b) ten-times yields (c). The recursion profiles are similar with each other despite the scale difference.

In Fig.7, we depicted the frequency distribution of a recurrent time τ_{rec} for core particles and halo particles separately. For core particles, as we expected, we find almost Gaussian distribution around the center $\tau_{\text{rec}} = \tau_{\text{R}}$ (Fig.7(a)). On the other hand for halo particles, although a peak is found around $\tau_{\text{rec}} = \tau_{\text{R}}$, the distribution shows a long tail spreads widely characterized by the power law $f(\tau_{\text{rec}}) \propto \tau_{\text{rec}}^{-p}$ with $p = 2.0$ (Fig.7(b)). We have checked that this power law range $3 < \log \tau_{\text{rec}} < 1.5$ is consistent with the eye-estimated region of self-similar motion in Fig.6. We will see that the above difference of frequency distribution for core and halo particles leads the difference in relaxation times for them in Sec.V.

We have also examined the energy dependence of the above power p . The result is given in (Fig.7) showing that the value of p (2.0) is almost independent of the choice of the energy U throughout the intermediate energy phase.

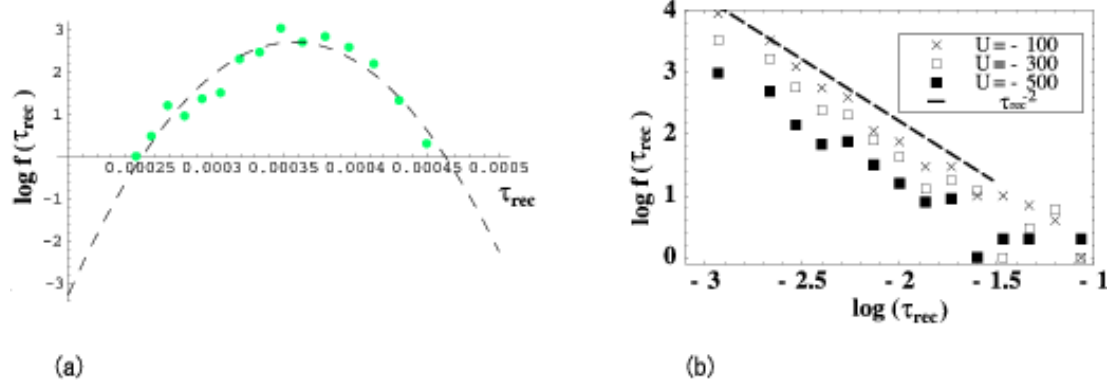


FIG. 7. A linear-log plot of frequency distribution $f(\tau_{\text{rec}})$ for core particles and a logarithmic plot of frequency distribution $f(\tau_{\text{rec}})$ for halo particles in several values of U . Each plot in (b) shows the same slope within the range $10^{3.0} < \tau_{\text{rec}} < 10^{1.5}$. The broken line represents a line with slope -2.0 .

B. Velocity distribution of particles

As is shown in Appendix A, the time averaged kinetic energy hK_i is, in general, expressed as the sum of N^2 independent stochastic variables. However, in the case of core particles, which are located within few cuto scale, the quantity hK_i turns out to be expressed as the sum of N independent stochastic variables (see Appendix B). In this section, we show that the N -dependence of hK_i characterizes the velocity distribution of particles.

In Fig. 8, we show the velocity distributions of core and halo particles in three cases; (a) $5 \times 10^4 R$, $U = 100$ (b) $5 \times 10^4 R$, $U = 500$ and (c) $5 \times 10^8 R$, $U = 0.65$. We have superposed the velocity data at $t = 1, 2, \dots, 5$, with ten different random initial conditions fixing the total energy. Thus the size of the whole data we used is 5×10^3 for each velocity distribution function. The distribution of core particles is well fitted by the Gaussian distribution

$$P(v) = \frac{1}{\sqrt{2\pi}} e^{-\frac{v^2}{2}}; \quad (4.2)$$

with the dispersion $v_{\text{core}}^{1/2} = 7.29$ (a); 10.9 (b) and 0.51 (c).

On the other hand, the distribution of halo particles in (a) is manifestly non-Gaussian, although its counterpart in (c) is Gaussian. This distribution is unchanged until 200 at least.

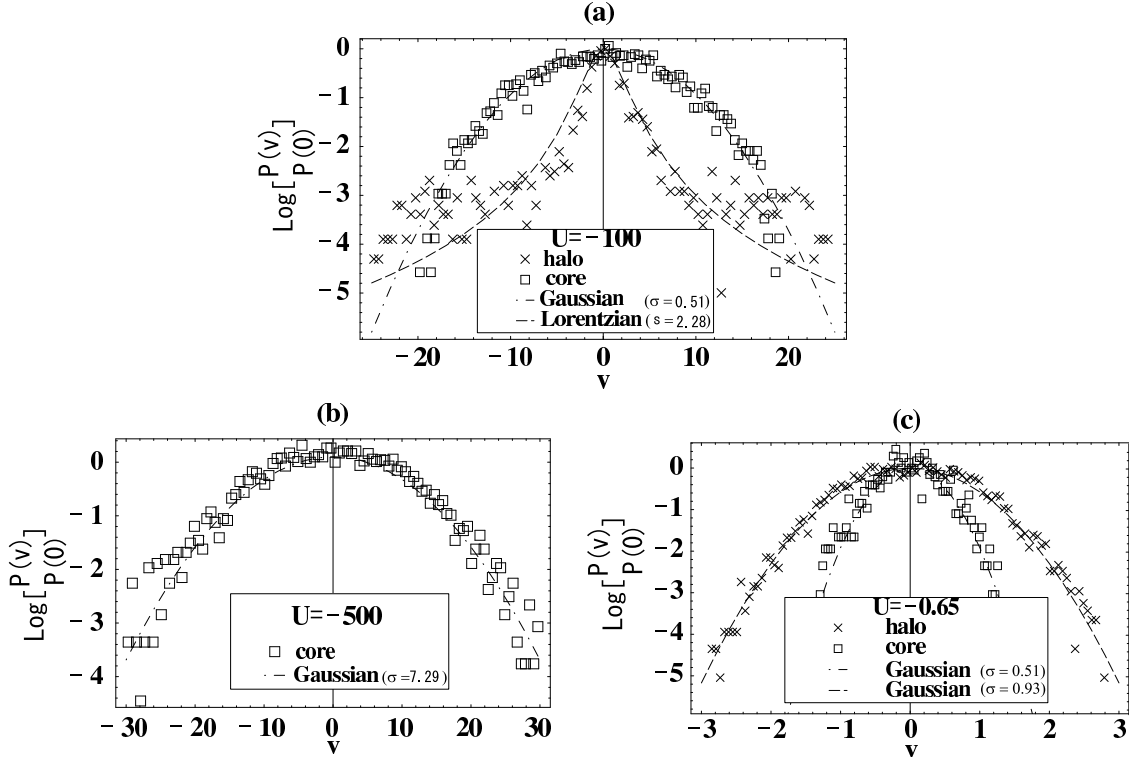


FIG. 8. The linear-log plot of velocity distributions of particles for the three cases; (a) $= 2.5 \cdot 10^7$, $U = -100$ (I-phase), (b) $= 2.5 \cdot 10^7$, $U = -500$ (C-phase), and (c) $= 2.5 \cdot 10^3$, $U = -0.65$ (I-phase). In all cases, velocities of core particles are well fitted by the Gaussian distribution with dispersion $= 0.51$ (a), 7.29 (b), and 0.51 (c) respectively. Also in the large cut-off case (c), velocities of halo particles are well fitted by the Gaussian distribution $= 0.93$. On the other hand, in the small cut-off case (a), velocities of halo particles are well fitted by the Lorentzian distribution ($= 1$) with $s = 2.2$.

What is the origin of the above non-Gaussian distribution for halo particles in the intermediate energy phase in case (a)? Here we analyze this issue from the viewpoint of the generalized central-limit theorem. It is well known that the limit distribution for sum s of independent random variables is the Gaussian distribution provided that the dispersion is finite (the central-limit theorem). However, it is less well-known that the limit distribution for sum s of independent random variables is the stable distribution in general case including the dispersion is divergent. This stable distribution is defined to satisfy the relation

$$\lim_{N \rightarrow \infty} \frac{1}{N} \sum_{i=1}^N x_i^N = \text{stable distribution} \quad (4.3)$$

where $\stackrel{d}{=}$ means that the distributions of both sides are equal to each other. The parameter α classifies the stable distributions and α must satisfy $0 < \alpha < 2$ for the normalization and the positivity of the probability distribution function. In the above, x_i and x are the probabilistic variables obeying the same distribution. Let us apply this to velocity distribution of our model. We square both sides of the above equation, and obtain the non-extensive property,

$$\langle v^2 \rangle_{N \text{ particles}} = N^{2-\alpha} \langle v^2 \rangle_{\text{one particle}} \quad (4.4)$$

and the method of characteristic function yields the explicit form of the distribution function [19]

$$P(v) = \frac{1}{2} \int_{-\infty}^{\infty} dy \exp[-ivy - s|y|]: \quad (4.5)$$

Note that this stable distribution includes the Gaussian distribution (4.2) as a special case $\beta = 2$; the kinetic energy becomes extensive, and the dispersion $\sigma^2 = 2s^2$ is finite. The parameter s is thought to be a generalized temperature.

Let us first consider the velocity distributions of core particles. We observe, from our numerical calculations, that all core particles oscillate within the narrow region of the cut-off size, and the gravitational two-body interaction is dominated by the artificial potential force. Therefore the averaged kinetic energy is described as the sum of N independent statistical elements (Appendix B). This leads the non-extensivity for the velocity distributions of core particles and therefore we expect the Gaussian distribution. This is consistent with the results in Fig.8.

On the other hand for halo particles which interact through genuine gravity, the kinetic energy behaves as $\langle K_{\text{p}} \rangle \propto N^2$ for fixed R as is shown in Appendix A. Thus we find the index $\beta = 1$ for the physical velocity distribution of SGR. In this case with $\beta = 1$, the distribution (4.5) becomes a Lorentz form

$$P(v) = \frac{1}{\sqrt{v^2 + s^2}} : \quad (4.6)$$

This is consistent with the results in Fig.8. The essence of the appearance of this non-Gaussian distribution is the non-extensivity of the energy for SGR; the intrinsic property of gravity.

What is the origin of the Gaussian distribution of halo particles in case (c)? As we show in next section, this is mainly because of the degeneration of a relaxation time between core particles and halo particles. In next section, we will discuss the relation between the profile of velocity distribution and a relaxation process.

V. RELAXATION

One of the most important issues in statistical physics of N -particle system is relaxation. In order to study such a relaxation process of our model, we choose several different initial conditions for the same values of β and U . Here we have examined two models, i.e. (i) $\beta = 2.5 \times 10^3$; $U = 0.65$ and (ii) $\beta = 2.5 \times 10^7$; $U = 100$, for both of which the negative specific heat appears.

As we discussed in Sec. II, there are three dynamical time scales: t_R , t , and t_E . In the units of our normalization, the ratios of these time scales are

$$\begin{aligned} t_E/t_R &= \frac{1}{\beta} \frac{1}{2} U^{1/2} \\ t/t_R &= (2)^{3/4} : \end{aligned} \quad (5.1)$$

For example, $t_E/t_R = 1.8 \times 10^4$ for $U = 100$, for which the specific heat is negative in the case with $\beta = 2.5 \times 10^7$. Moreover, $t/t_R = 1.88 \times 10^5$ for $\beta = 2.5 \times 10^7$. So if we take $U = 100$ and $\beta = 2.5 \times 10^7$, three time scales are separated as

$$t < t_E < t_R : \quad (5.2)$$

So, the contribution of gas particles to the dynamics of halo or core particles is negligible during a few t_R .

(i) does not meet the condition (3.3) and the $t_E/t_R = 0.34$. So t_E is the same order as t_R in (i). On the other hand, (ii) meets (3.3) and the $t_E/t_R = 1.8 \times 10^4$. So t_E is much shorter than t_R in (ii). This means that gas species play an important role in relaxation in case (i), while they do not in case (ii). In order to examine the relaxation process for these two cases, it is convenient to measure time with the unit t_E , since the relaxation of 3-D gravitational system is conventionally measured with the dynamical time. So here we introduce the dimensionless time $\tau = t/t_E$. From (5.1), the value of τ corresponding to t_E is obviously derived as

$$= \frac{1}{\beta} \frac{1}{2} U^{1/2} \tau : \quad (5.3)$$

As for initial conditions, we locate several clusters with the same interval. Each of them is composed of the same number of particles located at the same position. The number of clusters is chosen as 5, 10,

20, 25, and 50 for the model (i) and 5, 10, 20, and 25 for the model (ii). The initial velocities of particles are given randomly, so as to make the total energy the same value, $U = 0.65$ for (i) and $U = 100$ for (ii).

We examined the accumulative time duration of three states for each particle during the time interval of simulation, as follows. First, we pick up several discrete moments ($E_1; E_2; \dots; E_i; \dots$), where $E_0 + i \Delta E$ with the interval ΔE . Then we count the number of the moments between E_1 and E_i at which k 'th particle belongs to core, halo and gas state, respectively. Finally, by dividing each of the numbers by the total number of the moments, i , we can derive the proportion of three states $k_{\text{core}}(E_i); k_{\text{halo}}(E_i)$ and $k_{\text{gas}}(E_i)$ for k 'th particle up to the moment E_i .

At the first moment E_1 , all particles belong to one of the three states. So the proportion of three states for each particle, $k_{\text{core}}(E_1); k_{\text{halo}}(E_1)$ and $k_{\text{gas}}(E_1)$ are either 1 or 0. In the next moment E_2 , some of the particles may shift the state, then $k_{\text{core}}(E_2); k_{\text{halo}}(E_2)$ and $k_{\text{gas}}(E_2)$ for those particles will change the value into 0.5. As this procedure is repeated, $k_{\text{core}}(E_i); k_{\text{halo}}(E_i)$ and $k_{\text{gas}}(E_i)$ have more and more different values. So, we can see the time evolution of the distribution $N(\text{gas}; E)$, $N(\text{halo}; E)$ and $N(\text{core}; E)$, where $N(\text{gas}; E), N(\text{halo}; E)$ and $N(\text{core}; E)$ show the number of the particles which take the value core, gas and halo, respectively at the moment E . As the system is thermally relaxed and the equipartition of energy is attained, $k_{\text{core}}(E); k_{\text{halo}}(E)$ and $k_{\text{gas}}(E)$ for all k 's will converge to the same value core, halo and gas independent of the particle number k . Then $N(\text{gas}; E), N(\text{halo}; E)$ and $N(\text{core}; E)$ would have sharp peaks at core, halo and gas in the thermal equilibrium state. So we can roughly judge whether or not the system approaches the thermal equilibrium state by seeing the time evolution of $N(\text{gas}; E), N(\text{halo}; E)$ and $N(\text{core}; E)$.

In case (i), the distribution $N(\text{gas}; E), N(\text{halo}; E)$ and $N(\text{core}; E)$ starting from $E_0 = 6.5 \times 10^4$ has one peak between 0 and 1 at least by the time $E = 10^5$ (Fig. 9 (b)) and the variance around the peak becomes smaller and smaller (Fig. 9 (c)). Then almost all particles experience all of the three states at least by $E = 2.0 \times 10^5$. This means the thermal relaxation proceeds in the time scale $E = 10^5$ in case (i). In case (ii), in contrast, the distribution $N(\text{gas}; E), N(\text{halo}; E)$ and $N(\text{core}; E)$ starting from $E_0 = 1.1 \times 10^5$ has its own peaks at either 1 or 0 even after the time duration, $E = 3.8 \times 10^5$ (Fig. 9 (e)). So most particles stay in one state even in the time scale $E = 10^5$ in case (ii). So we can say that the system does not approach the thermal relaxation at all during this time scale in this case.

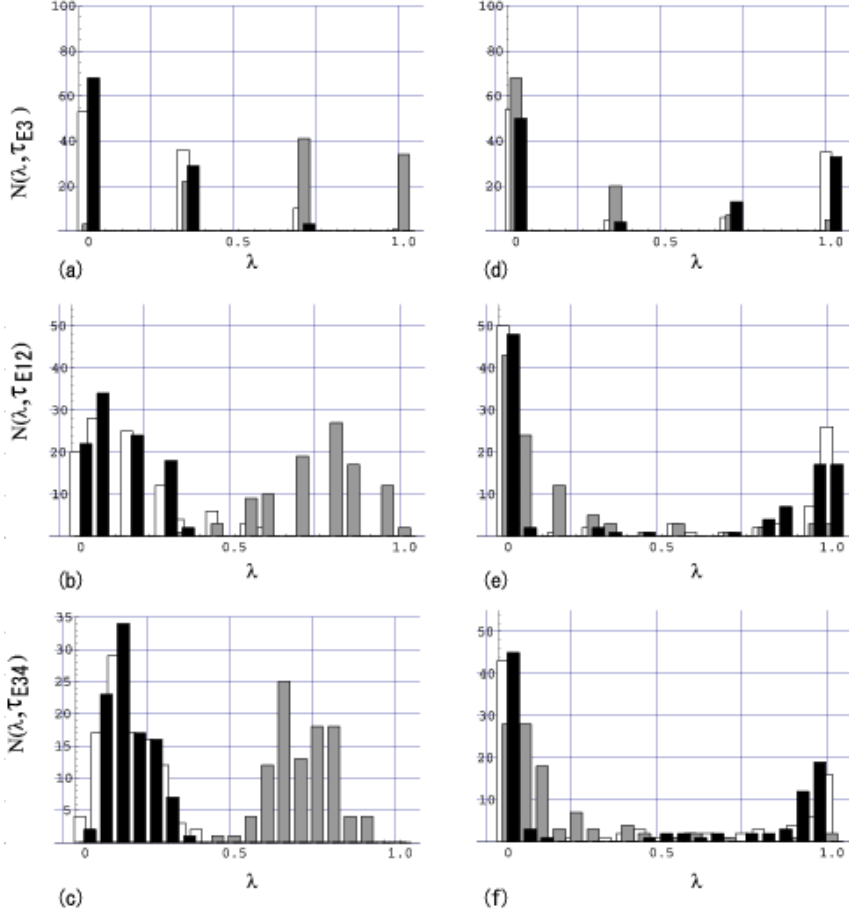


FIG. 9. The time variation of $N(\lambda, \tau)$, where the bar in white, gray and black colors show $N(\text{gas}; E)$, $N(\text{halo}; E)$ and $N(\text{core}; E)$, respectively. The left and right figures represent the case with (i) $E_0 = 2.5 \times 10^3$ and $U = 0.65$ and (ii) $E_0 = 6.5 \times 10^4$ and $U = 100$, respectively, where $E_0 = (i) 6.5 \times 10^4$ and (ii) 1.1×10^5 and $E = (i) 2.0 \times 10^3$ and (ii) 3.8×10^3 . The upper, middle and lower figures show the case at the moment E_i , where (i = 3; 12; 34), respectively.

By combining these results, it seems that the Gaussian velocity distribution of case (i) in Fig.8 reflects the thermal relaxation, while the Lorentzian velocity distribution of case (ii) in Fig.8 does not. We may conclude that the particle motions in halo species characterized by the Lorentzian velocity distribution for small λ are the features at quasi-equilibrium state, quite long before the system attains thermal relaxation. This peculiar properties may make 3-D gravitational system quite different from those in the system with short-range interactions or the system with positive specific heat. As λ approaches unity and halo particles encounter both gas and core particles so often, extracting such exotic characters of halo particles becomes more and more difficult. Hence, each species reach thermodynamic equilibrium state as in case (i).

VI. SCALING PROPERTIES OF THE HALO

In Sec.IV, we have found that the velocity distribution of halo particles is non-Gaussian with the v^2 -tail and each halo particle shows intermittent recursive motion around the core without a definite time scale. This scale-free property of the halo appears in the distribution profile of the halo particles itself. In this section, we study the scaling property of the distribution with the box-counting method [20].

For this purpose, we divide the entire configuration space $2R$ into segments with the equal size ' and count the number $N(')$ of the segment which contains at least one halo particle. Then we define the quantity $\theta(\log N(')) = \theta(\log ')$ which turns out to be the scaling exponent provided that the quantity

is almost independent of the scale ℓ and actually posses the scaling property. In the actual calculation, we need to increase the statistical significance. Therefore we used multiple particle-distribution data at different times for each run. Moreover we made many runs of calculations with different initial conditions for the fixed total energy U . We have applied the box-counting method to each data and then all the individual results are superposed. When we extract the distribution data, we have chosen the time interval $[2000t; 5000t]$, in which the particle ratios core, halo, and gas almost reach the relaxed constant values. Thus we calculate the following averaged quantity

$$D(\ell) = \frac{\ell \langle \log N(\ell) \rangle}{\ell \langle \log \ell \rangle} ; \quad (6.1)$$

over all the data we thus prepared. If any scaling property exists in the particle distribution, $D(\ell)$ would become constant for a finite range of $\ell_1 < \ell < \ell_2$. As for the bounds ℓ_1 and ℓ_2 , we have technical restrictions originates from our numerical calculation method. The averaged distance between gas particles is estimated as

$$l_{\text{gas}}(\ell) = \frac{2R}{N_{\text{gas}}} ; \quad (6.2)$$

If the box size ℓ is larger than $l_{\text{gas}}(\ell)$, we expect $D \approx 1.0$, because almost all the boxes contain at least one particle. On the other hand, if ℓ is smaller than the cut-off distance l_{gas} , genuine property of gravity is lost. Therefore if the gravitational interaction yields the scaling property in particle distribution, the scaling range $\ell_1 < \ell < \ell_2$ would be significant if $\ell_1 > l_{\text{gas}}$ and $\ell_2 < l_{\text{gas}}$. Actually in our calculation, for $\ell = 2.5 \times 10^7$ and $U = 100$, we can see the typical behavior of $N(\ell)$ as a function of ℓ in Fig.10. In this picture, we can see the scaling behavior $N(\ell) \sim \ell^d$ with the small exponent in the range $10^3 R < \ell < 10^1 R$, which is well inside the significant region. This scaling seems to originate from halo particles, because they not only dominate in the above scaling range but also show non-Gaussian velocity distributions and self-similar recursion jumps.

However, the above result of the box counting method does not directly conclude the existence of the fractal structure in the particle distributions. This is because the box counting method itself cannot distinguish the two possibilities; a) genuine fractal structure from b) the power-law tail of the particle distributions around the core center.

In order to distinguish the above possibilities, we try and compare two different superposition methods as follows. We have already prepared many data set obtained from our numerical calculations with the method mentioned above. The superposition methods are a) simply superpose all the data with the bare coordinate and b) superpose all the data with the coordinate adjusting so that the mass-center of each data comes to the same position; i.e. we introduce a new coordinate as ℓ_{bc} for each data with the mass center ℓ_{bc} .

As a result, the scaling property of the particle distributions, which was observed in the original method, disappears completely in the case a). On the other hand in the case b) we observe the same scaling property as was observed in the original method. This result suggests that the observed scaling property in particle distribution is not the genuine fractal property of the system, but simply due to the power-law distribution of particles around the mass-center. We have confirmed this with our further analysis on the direct observation of the power-law particle distributions around the mass-center.

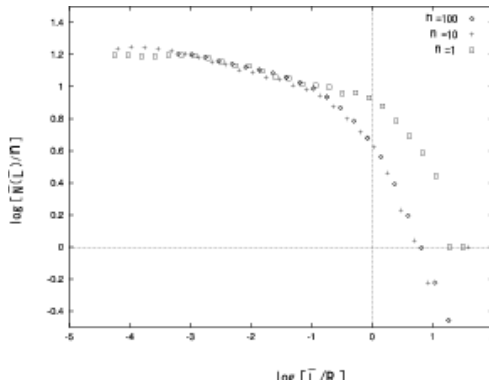


FIG. 10. Log-log plot for the box scale L vs the number of the box N occupied by at least one halo particle by use of superposed data with n different time. The case with $n = 1, 10$ ($\epsilon_0 = 2.0; \epsilon = 0.3$), and 100 ($\epsilon_0 = 2.0; \epsilon = 0.03$) for the cuto $\epsilon = 2.5 \cdot 10^{-7}$ where $R = 10^3 R$ are plotted. The data points in these three cases are overlapped in the range of $10^{-1} < L < 10^1 R$. The scaling exponent $D(L)$ derived from the slope in this range is 0.1.

The energy and cuto dependency of the scaling exponent D is shown in Fig. 11. Here we show the scaling exponent of halo particles in the negative energy region. We find that the scaling exponent D is almost constant in the region of the negative specific heat. Moreover, smaller the cuto ϵ , smaller the exponent D . On the other hand in the limit of $\epsilon \rightarrow 0$, the scaling property cannot be observed in principle since the range of L becomes too small to exhibit the scaling structure.

In the limit of a real gravitational interaction ($\epsilon \neq 0$), the region of the negative specific heat extends in energy range and does the scaling region. This universality is likely to be independent of the temperature or the energy of the system.

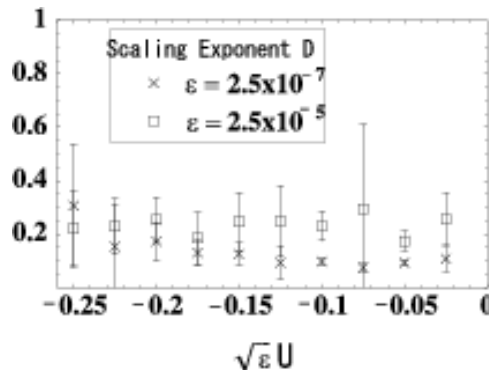


FIG. 11. The scaling exponent D vs the energy per particle U . A most of the energy region shown in the figure corresponds to I-phase. For the convenience, we use $\sqrt{\epsilon} U$ as a horizontal axis. The case of $\epsilon = 2.5 \cdot 10^{-5}$ (square with error bars) and the case of $\epsilon = 2.5 \cdot 10^{-7}$ (cross with error bars) are plotted. It seems that the dimension D does not depend on U . Since the number of halo particles is small in the low energy, the error becomes large.

VII. CONCLUSION

In this paper we have studied self-gravitating ring (SGR) model which is an one-dimensional (1-D) toy model of a self-gravitating system. Although the system is 1-D, the particles constrained on a circular ring mutually interact with the 3-D full gravitational force. We found that an interesting phase with the negative specific heat appears at the intermediate energy scale, which reflects the virial condition of a 3-D gravitating system. Classifying the particles in each phase into three species (core, halo, and gas species), this phase is characterized by the halo particles. Using SGR, we have examined characteristic properties of relaxation, velocity distributions, and density profiles in each phases.

The cuto parameter introduced in SGR model controls the singular properties of the system at short-distances. By changing this parameter, we could systematically study the effect of the short-distance singularity of the force upon the statistical properties of the system.

When the cuto parameter is of order one ($\epsilon \sim R$), the system resembles the Hamiltonian mean-field model (HMF). In fact, the velocity distribution becomes Gaussian at $t \gg 0$ (t_R) for HMF. This is because t_E and t_R are in the same order and therefore halo particles often encounter and interact with gas particles. This strong interaction induces frequent exchange of particles between these two species. Thus the energy diffuses effectively and the entire thermodynamical equilibrium establishes. In other words, particles with the negative specific heat do exist but the strong interaction with gas and core particles dissolves the negative specific heat region.

In our examined case with $\epsilon = 7.1 \cdot 10^2 R$ ($\epsilon = 2.5 \cdot 10^3$), the velocity distribution becomes almost Gaussian after it is settled to the virialized state, although the temperature of each species is different.

from each other. In larger value of α almost equal to 1, the differences among different species would disappear and reach thermal equilibrium more quickly.

On the other hand, as $\alpha \neq 0$, the two time scales becomes $t_R \ll t$, and the energy region of the negative specific heat extends wider. Therefore we can expect that halo particles become almost independent of gas particles. This isolation of halo particles from other species enables this unstable halo species to last sufficiently longer. In our examined case with $\alpha = 7:1 \cdot 10^4 R$ ($\alpha = 2:5 \cdot 10^7$), the initial condition dependence of halo particles survives even after $5 \cdot 10^4$ in our simulation, which prevents the full system from reaching a thermal equilibrium state. This results resemble the case of core particles with $\alpha = 7:1 \cdot 10^2 R$. However, the remarkable difference between the two cases is that the velocity distribution of halo particles in $\alpha = 7:1 \cdot 10^4 R$ shows non-Gaussian features and follows the Lorentzian distribution, while those of core particles in $\alpha = 7:1 \cdot 10^4 R$ follow Gaussian. This property of halo particles qualitatively reflects genuine 3-D gravitational systems and is the main difference from the HMF models and 1D S models without short-distance singularity. We have also found the scaling structure of halo particles in the intermediate energy phase. In the gravitational limit, $\alpha \neq 0$, both the energy range with negative specific heat and the scaling region are also extended, although the value of exponent depends on the cut-off and decreases with α .

In 1D S model, the system reaches the thermal equilibrium at least at $t \approx 0(10^7)t_E$, where $t_E = (1/4 \cdot G \cdot m \cdot N)^{1/4} \cdot E = m \cdot N$ is the crossing time of 1D S [11]. It is also shown that the system reaches the collisionless mixing phase during much shorter time interval. Our simulation with $\alpha = 7:1 \cdot 10^4 R$ shows non-Gaussian velocity and scaling property in such a short time interval $4 \cdot 10^3 t_E \approx 2 \cdot 10^8 t_E$ for $U = 100$. So the non-Gaussian velocity distribution might reflect the character in collisionless mixing phase which appears in 1D S simulation [11]. However, it might also be true that the relaxation process in SG R is quite different from that in 1D S, where no time scale separation between core and halo particles exists. So the exotic character of halo particles might be intrinsic in SG R or the system with real 3-D gravitational interactions because of the time scale separation.

As for the comparison with observations, exotic non-Gaussian statistics of halo particles may play an important role in determining the conformation of astrophysical objects such as galaxies or dark matters around them. For example, the recent observations with Hubble Space Telescope support the existence of supermassive black holes or cusps at the center of most elliptical galaxies [22-24]. So the time scale separation which appears in SG R is expected in observed elliptical galaxies, since they have high density regions which correspond to core species at their centers. So, the time scale separation which we showed in our SG R model might give the hint for the relaxation process of elliptical galaxies which are not relaxed with two-body interactions between element stars within the age of our universe. In addition, the model might be helpful to explain the observed fractal structures and non-Gaussian velocity distributions in the interstellar medium [25], since they are gravitationally virialized.

ACKNOWLEDGMENTS

We would like to thank A. Nakamichi, I. Joichi, K. Nakamura, and M. Hotta for useful discussions and comments. This work was supported partially by a Grant-in-Aid for Scientific Research Fund of the Ministry of Education, Science and Culture (Specially Promoted Research No. 08102010), and by the Waseda University Grant for Special Research Projects.

APPENDIX A: VARIOUS CONDITIONS FOR SG R MODEL

We start with the normalized Hamiltonian,

$$H = \frac{1}{2} \sum_{i=1}^{N^2} p_i^2 - \frac{1}{2N} \sum_{i < j} \frac{1}{1 - \cos \theta_{ij}} = 0 \quad (A1)$$

Canonical equations for this Hamiltonian become

$$\frac{d \dot{p}_i}{dt} = p_i;$$

$$\frac{dp_i}{d} = \frac{x^N}{2} \frac{p}{2N} \frac{\sin_{ij}}{(1 - \cos_{ij})^{3/2}}; \quad (A 2)$$

So, the second time derivative of inertia moment of this system becomes

$$\begin{aligned} \frac{d^2}{d^2} \frac{x^N}{2} \frac{p}{2N} \frac{\sin_{ij}}{(1 - \cos_{ij})^{3/2}} &= 2 \frac{x^N}{2} \frac{p}{2N} \frac{d_i}{d} + \frac{x^N}{2} \frac{p}{2N} \frac{dp_i}{d} \\ &= 2 \frac{x^N}{2} \frac{p^2}{2N} \frac{2}{i < j} \frac{\frac{x^N}{2} \frac{p}{2N} \frac{i \sin_{ij}}{(1 - \cos_{ij})^{3/2}}}{(1 - \cos_{ij})^{3/2}}; \end{aligned} \quad (A 3)$$

The time averaging for this relation becomes

$$\frac{d^2}{d^2} \frac{x^N}{2} \frac{p}{2N} \frac{\sin_{ij}}{(1 - \cos_{ij})^{3/2}} = 4N T \frac{2}{i < j} \frac{x^N}{2} \frac{p}{2N} \frac{i \sin_{ij}}{(1 - \cos_{ij})^{3/2}} + ; \quad (A 4)$$

So if

$$I(\cdot) = \frac{d^2}{d^2} \frac{x^N}{2} \frac{p}{2N} \frac{\sin_{ij}}{(1 - \cos_{ij})^{3/2}} = (N T) - 1; \quad (A 5)$$

the virial condition

$$T = \frac{1}{2N} \frac{x^N}{2} \frac{p}{2N} \frac{i \sin_{ij}}{(1 - \cos_{ij})^{3/2}} + ; \quad (A 6)$$

is satisfied.

By using the total potential

$$V = \frac{x^N}{2} \frac{p}{2N} \frac{p}{1 - \cos_{ij}} + ; \quad (A 7)$$

The virial condition (A 6) can be expressed as

$$T = \frac{1}{2N} \frac{x^N}{2} \frac{i \frac{\partial V}{\partial i}}{1 - \cos_{ij}} + ; \quad (A 8)$$

Note that even in the limit of $i = 2N T = hV$ $i=2$ is not justified, because of the potential form (A 7). However, as is shown in Sec. II, we can get the above ideal virial condition for 3-D gravity within the appropriate energy range.

APPENDIX B: VIRIAL CONDITION IN A C-PHASE FOR SGR MODEL

In C-phase, almost all of the particles are trapped inside core whose size is almost $1/N$. So in this state canonical equations (A 2) are approximated as

$$\begin{aligned} \frac{d_i}{d} &= p_i; \\ \frac{dp_i}{d} &= \frac{x^N}{2} \frac{p}{2N} \frac{ij}{(1 - \cos_{ij})^{3/2}} \\ &= \frac{p_i}{2} \frac{1}{2^{3/2}} - \frac{1}{N} + \frac{x^N}{2} \frac{p}{2N} \frac{j}{(1 - \cos_{ij})^{3/2}}; \end{aligned} \quad (B 1)$$

since $j_{ij}j \propto 0(1)$.

In this approximation, the second time derivative of inertia moment of this system becomes

$$\frac{d^2}{dt^2} \sum_i \frac{x_i^2}{p_i^2} = 2 \sum_i \frac{1}{N} \frac{x_i^N}{p_i^2} + \frac{2}{2N} \sum_{i < j} \frac{x_i^N}{p_i^2} \quad (B2)$$

The time averaging for this relation becomes

$$\frac{d^2}{dt^2} \sum_i \frac{x_i^2}{p_i^2} = 4N T \sum_i \frac{1}{N} \frac{x_i^N}{p_i^2} + \frac{2}{2N} \sum_{i < j} \frac{x_i^N}{p_i^2} \quad (B3)$$

Since x_i and x_j ($i \neq j$) are independent stochastic variables, the last term of (B3) should be omitted. Hence from the virial condition,

$$T = \frac{1}{4} \frac{1}{2N} \sum_i \frac{x_i^2}{N} \quad (B4)$$

and

$$hK_{pi} = \frac{G m^2}{2^2} \sum_i \frac{x_i^N}{N} \quad (B5)$$

are satisfied. This shows that hK_{pi} in C-phase is derived as the sum of N statistical elements.

- [1] W. H. Zurek, P. J. Quinn, J. K. Salmon, and M. S. Warren, *Astrophys. J.* 431 (1994) 559.
- [2] F. Sylos Labini, M. Montuori, and L. Pietronero, *Phys. Rep.* 293 (1998) 61.
- [3] G. de Vaucouleurs, *Science* 167 (1970) 1203.
- [4] H. J. de Vega, N. Sanchez, and F. Combes, *Phys. Rev. D* 54 (1996) 6008.
- [5] V. A. Antonov, *Vest. Leningr. Gos. Univ.* 7 (1962) 135.
- [6] D. Lynden-Bell and R. Wood, *Mon. Not. R. Astr. Soc.* 138 (1968) 495.
- [7] I. Hachisu and D. Sugimoto, *Prog. Theor. Phys.* 60 (1978) 123.
- [8] E. B. Alanson and C. J. Hansen, *Astrophys. J.* 177 (1972) 145.
- [9] D. Lynden-Bell, *Mon. Not. R. Astr. Soc.* 136 (1967) 101.
- [10] G. L. Camm, *Mon. Not. R. Astr. Soc.* 110 (1950) 305.
- [11] T. Tsuchiya, N. Gouda, and T. Konishi, *Phys. Rev. E* 53 (1996) 2210.
- [12] M. Antoni and S. Rufo, *Phys. Rev. E* 52 (1995) 2361.
- [13] V. Latora, A. Rapisarda, and S. Rufo, *Phys. Rev. Lett.* 83 (1999) 2104.
- [14] T. Padmanabhan, *Phys. Rep.* 188 (1990) 285.
- [15] P. Hertel and W. Thirring, *Annals of Physics* 63 (1971) 520.
- [16] A. Compagner, C. Bruun, and A. Roelse, *Phys. Rev. A* 39 (1989) 5989.
- [17] Y. Aizawa, K. Sato, and K. Ito, *Prog. Theor. Phys.* 103 (2000) 519.
- [18] M. Suzuki, *Phys. Lett. A* 146 (1990) 319.
- [19] W. Feller, *An Introduction to Probability Theory and Its Applications* 2nd ed. (Wiley & Sons, Inc. New York, 1966), Vol. II.
- [20] K. Falconer, *Fractal Geometry* (John Wiley & Sons, 1990).
- [21] J. Binney and S. Tremaine, *Galactic Dynamics* (Princeton Series of Astrophysics, 1987).
- [22] T. R. Lauer et al, *Astrophys. J.* 110 (1995) 2622.
- [23] T. R. Lauer et al, *Astrophys. J.* 111 (1996) 1889.
- [24] K. G. Ebdhardt et al, *Astrophys. J.* 112 (1996) 105.
- [25] E. Falgarone, T. G. Phillips, and C. K. Walker, *Astrophys. J.* 378 (1991) 186.